North Atlantic Summertime Anticyclonic Rossby Wave Breaking: Climatology, Impacts, and Connections to the Pacific Decadal Oscillation

BREANNA L. ZAVADOFF AND BEN P. KIRTMAN

Rosenstiel School of Marine and Atmospheric Science, University of Miami, Miami, Florida

(Manuscript received 16 May 2018, in final form 14 November 2018)

ABSTRACT

Anticyclonic Rossby wave breaking (RWB) is characterized by the rapid and irreversible deformation of potential vorticity (PV) contours on isentropic surfaces manifesting as a pair of meridionally elongated high- and low-PV tongues that transport extratropical stratospheric air equatorward and tropical tropospheric air poleward, respectively. Previous studies have noted connections between different types of RWB and the modulation of localized atmospheric phenomena such as the North Atlantic Oscillation (NAO) and tropical cyclogenesis. Despite being the season in which anticyclonic RWB events are most prevalent, no work has focused solely on the frequency, genesis, or variability of the synoptic environment surrounding the equatorward branch of anticyclonic RWB events during the North Atlantic summertime, providing motivation for this study. Using 58 years (1960–2017) of NCEP–NCAR reanalysis data, a comprehensive spatiotemporal climatology of North Atlantic equatorward anticyclonic RWB identified on the 350-K isentropic surface is developed and the synoptic environment surrounding these events from time- and high-PV-tongue centroid-relative perspectives is investigated. Consistent with previous studies, composites suggest that high-PV tongues associated with equatorward anticyclonic RWB introduce anomalously dry, stable extratropical air into the tropical environment, subsequently inhibiting convection there. Additionally, a connection between atmospheric responses to Pacific decadal oscillation (PDO) sea surface temperature (SST) anomalies and the intrabasin frequency of anticyclonic RWB events is uncovered and explored. Results from this study may aid short- to medium-range forecasts of North Atlantic tropical convection, with applications extending into the field of tropical cyclogenesis forecasting.

1. Introduction

Rossby wave breaking (RWB), from the "potential vorticity (PV) theta" perspective, is characterized by the rapid and irreversible deformation of PV contours on isentropic surfaces (McIntyre and Palmer 1983, 1984). When RWB occurs in the upper troposphere–lower stratosphere, the isentropic surfaces on which the waves are breaking intersect the tropopause, resulting in a quasi-horizontal mixing of stratospheric and tropospheric air (Holton et al. 1995; Scott and Cammas 2002). McIntyre and Palmer (1983, 1984) identified areas in which RWB occurs most, if not all, of the time, dubbed "surf zones," regions where large-scale PV gradients and time-mean winds are relatively weak (Peters and Waugh 1996; Postel and Hitchman 1999, 2001; Scott and Cammas 2002). The weak time-mean winds in the surf zones serve as Rossby wave critical lines where the zonal phase speed of a wave matches the mean zonal flow speed. When propagating Rossby waves approach their critical lines they "pile up," causing their phase lines and associated PV contours to transform into a zonally elongated, meridionally confined pattern indicative of breaking.

RWB events in the upper troposphere–lower stratosphere are described as equatorward or poleward in nature: the former depicted by tongues of high-PV stratospheric air extending equatorward into the troposphere (Hoskins et al. 1985; Thorncroft et al. 1993), while the latter exhibits opposing features with tongues of low-PV tropospheric air extending poleward into the stratosphere (Hoskins et al. 1985; Peters and Waugh 1996). The equatorward and poleward types of RWB can be further classified into paradigms corresponding to whether they exhibit cyclonic or anticyclonic characteristics. Modeling studies performed by Thorncroft et al. (1993) and Peters and Waugh (1996) revealed that the ambient meridional shear plays a role in determining how the waves will break (i.e., cyclonically or anticyclonically), whereas Gabriel and Peters (2008) found that a predominance of the

Corresponding author: Breanna L. Zavadoff, bzavadoff@rsmas.miami.edu

DOI: 10.1175/JCLI-D-18-0304.1

meridional wave fluxes in either the equatorward or poleward breaking branch dictates the RWB event's meridional direction classification. The four resulting paradigms of RWB are as follows: cyclonic poleward, anticyclonic poleward, cyclonic equatorward, and anticyclonic equatorward (hereafter referred to as anticyclonic RWB). Many climatological studies have been performed on the spatiotemporal distribution of all four paradigms of RWB (Postel and Hitchman 1999; Martius et al. 2007; Hitchman and Huesmann 2007; Wernli and Sprenger 2007; Gabriel and Peters 2008). Consistent findings among these studies include the preference for cyclonic equatorward RWB to occur on lower isentropic levels than anticyclonic RWB, a predominance for cyclonically sheared events to occur at higher latitudes over Iceland in the Atlantic and the Aleutian Islands in the Pacific, and that anticyclonically sheared events occur most commonly over the midlatitude subtropical oceans. Additionally, RWB frequency has been found to be modulated by El Niño–Southern Oscillation (ENSO), such that during the warm (cold) phase, the eastward (westward) extension of the subtropical jet facilitates an environment favorable to increase the frequency of cyclonic (anticyclonic) RWB over the eastern Pacific (Martius et al. 2007).

RWB events have been closely linked to the North Atlantic Oscillation (NAO; Benedict et al. 2004; Franzke et al. 2004; Strong and Magnusdottir 2008) such that anticyclonic (cyclonic) RWB precedes and maintains a positive (negative) NAO, atmospheric blocking in the Northern Hemisphere (Tyrlis and Hoskins 2008), and heavy precipitation events over Europe (Massacand et al. 1998; Martius et al. 2006). While these phenomena are all isolated to the extratropics, RWB can have far-reaching impacts on tropical convection as well, primarily through interactions between the high-PV tongue associated with anticyclonic RWB and the tropical environment (Kiladis and Weickmann 1992; Knippertz 2007; Allen et al. 2009). Recent studies by Zhang et al. (2016, 2017) show that RWB can affect tropical cyclone (TC) development, noting that summertime anticyclonic RWB events lead to the suppression of TC activity via the intrusion of enhanced vertical wind shear, subsidence, and dryness. A reduction in TC formation has been shown to be especially true for years where there is a high frequency of anticyclonic RWB events in the western half of the Atlantic basin (Zhang et al. 2017).

Even though the Northern Hemisphere summer is the time at which anticyclonic RWB events are most prevalent, specifically during the months of June–September (Postel and Hitchman 1999), an overwhelming majority of studies have focused on wintertime high-latitude RWB variability and impacts. As previously mentioned, there are important implications to studying the variability of summertime midlatitude RWB events and how they modify the tropical environment with which they interact. The lack of literature regarding this topic is what drives the main objective of this paper: to establish a climatology of anticyclonic RWB events over the North Atlantic during boreal summer and analyze their effects on the surrounding synoptic environment. Anticyclonic RWB events have been chosen as the focus of this study, as cyclonic equatorward events are infrequent south of 40°N during boreal summer. Additionally, Zhang et al. (2017) note that the frequency and location of anticyclonic RWB events modulates the environmental variability of the tropical Atlantic and the TCs that develop there. Therefore, a secondary objective of this paper is to determine what mechanisms control the intrabasin frequency and location of North Atlantic anticyclonic RWB events.

The remainder of this paper is organized as follows. Section 2 outlines the datasets and methodology used to identify the anticyclonic RWB events. Section 3 describes the full and intrabasin climatologies of North Atlantic anticyclonic RWB events. Section 4 delves into the temporal and spatial characteristics of anticyclonic RWB events as well as their impacts on the surrounding synoptic environment. Section 5 explores a possible source of anticyclonic RWB event modulation. Section 6 will present the summary discussion of this study.

2. Data and methods

a. *RWB identification and climatology*

For this study, we utilize 58 years (1960–2017) of the National Centers for Environmental Prediction–National Center for Atmospheric Research (NCEP–NCAR) reanalysis dataset (Kalnay et al. 1996) on isentropic and isobaric surfaces. Fields are interpolated onto a 2.5° × 2.5° latitude–longitude grid and have a 6-h temporal resolution. Though RWB occurs on many other isentropes at other altitudes, PV on the 350-K isentropic surface is used to identify anticyclonic RWB events because of its closer proximity to the summertime subtropical tropopause than other isentropic surfaces (Abatzoglou and Magnusdottir 2006). Because of its positioning near the tropopause, anticyclonic RWB on the 350-K isentrope forces some of the largest interactions between the extratropical stratosphere and tropical troposphere (Postel and Hitchman 1999) and produces robust effects via mixing on the surrounding environment as compared to other isentropic surfaces. Because this study, in part, aims to describe how anticyclonic RWB affects the environment and breaking on the 350-K isentrope results in a significant amount of extratropical stratosphere–tropical troposphere mass exchange, the 350-K surface serves as the best choice for RWB identification.

The subtropical North Atlantic, defined here as the region lying within 10°–40°N, 10°–80°W, is the region over

which anticyclonic RWB detection will occur. This domain is chosen as it runs along and equatorward of the subtropical jet throughout the North Atlantic (Abatzoglou and Magnusdottir 2006), encompassing a region of ambient anticyclonic shear that is favorable for anticyclonic RWB (Thorncroft et al. 1993). Though results from this and previous studies such as Postel and Hitchman (1999) and Zhang et al. (2017) indicate that anticyclonic RWB preferentially occurs around 30°–35°N, the domain was extended as far south as 10°N to ensure any and all events were recorded. Once all the anticyclonic RWB events have been identified and recorded, isobaric surface data are used during postprocessing for centroid- and time-relative composite analyses.

A climatology is established using the algorithms described in Abatzoglou and Magnusdottir (2006) and Strong and Magnusdottir (2008) to identify high-PV tongues connected to an anticyclonic RWB event. Objective detection of an anticyclonic RWB event follows three main criteria, as outlined in Fig. 1:

- Reversal in the latitudinal PV gradient, such that a high-PV tongue (PV $\geq$ 3 PVU; 1 PVU = 10^{-6} K kg^{-1} m^2 s^{-1}) is located equatorward of a low-PV region (PV $\leq$ 1.5 PVU)
- A positive longitudinal PV gradient ($\partial \mathrm{PV}/\partial x > 0$) about the break, consistent with an anticyclonically sheared RWB event
- The high-PV tongue (low-PV tongue) is linked to a region of extratropical (tropical) PV

Despite the subjective selection of the latitudinal PV gradient reversal strength, chosen to ensure that anticyclonic RWB events with strong mixing are included in the dataset, varying the strength does not affect the distribution of our results, though it does affect the frequency in a manner to be expected, as discussed in section 3a. Additionally, for the third criterion, linkage between the high-PV tongue (low-PV tongue) and a region of extratropical (tropical) PV is ensured via manual inspection of all detected events. If the 3- (1.5-) PVU contour is observed to remain continuous around the entirety of the high-PV (low PV) tongue and is backed by higher (lower) values of extratropical (tropical) PV to the north (south), the criteria is satisfied and the event is recorded.

Further spatial and temporal criteria are also implemented to ensure any short-lived, longitudinally confined, latitudinal PV gradient reversals detected by the objective algorithm are discarded as they can be induced by scales of motion smaller than Rossby waves (Postel and Hitchman 1999). Therefore, latitudinal PV gradient reversals must cover a minimum longitudinal extent of 10° and be detected for a minimum of 18 consecutive hours to be recorded in the final dataset as an anticyclonic RWB event.

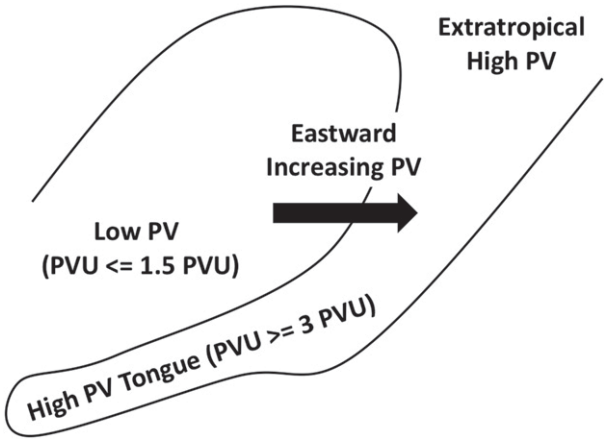

FIG. 1. Schematic illustration of the three criteria governing the objective anticyclonic RWB detection algorithm on the 350-K isentropic surface.

Seeing that the typical anticyclonic RWB event lasts 1–3 days and is thus flagged at multiple instances by the anticyclonic RWB detection algorithm, only a single time is recorded to represent the entire anticyclonic RWB event and avoid redundancy. As in Abatzoglou and Magnusdottir (2006), this time is selected when all the above criteria have been satisfied and the high-PV tongue reaches its southwesternmost extent. All other detections of the same anticyclonic RWB event are then discarded. Once the time is selected, the central point on the high-PV tongue at that time is identified and recorded as the centroid of the anticyclonic RWB event, which is used for centroid-relative composite analyses.

To supplement the full basin climatology, an intrabasin climatology is established by splitting the domain in half at the 45°W meridian into the east and west basin subdomains. An anticyclonic RWB event is classified as eastern basin (EB) if its centroid lies to the east of the 45°W meridian, while the converse is true for western basin (WB). If a centroid falls directly on the 45°W meridian, it is objectively classified into the subgroup in which the greatest area of the high-PV tongue is located.

b. *Centroid-relative composites*

Given the large spatial distribution of anticyclonic RWB events within the domain, composites of different environmental variable anomalies with respect to the centroid of the high-PV tongue are produced to most effectively capture how stratospheric intrusion into the tropical troposphere alters the local synoptic environment. Anomalies of various fields are calculated by removing long-term trends from the data and subtracting out the seasonal means from the anticyclonic RWB event environment at the corresponding locations around the centroid. Following the strategy used in Zhang et al. (2017) to ensure inclusion of the entire anticyclonic RWB event in the composite, a domain of 50°

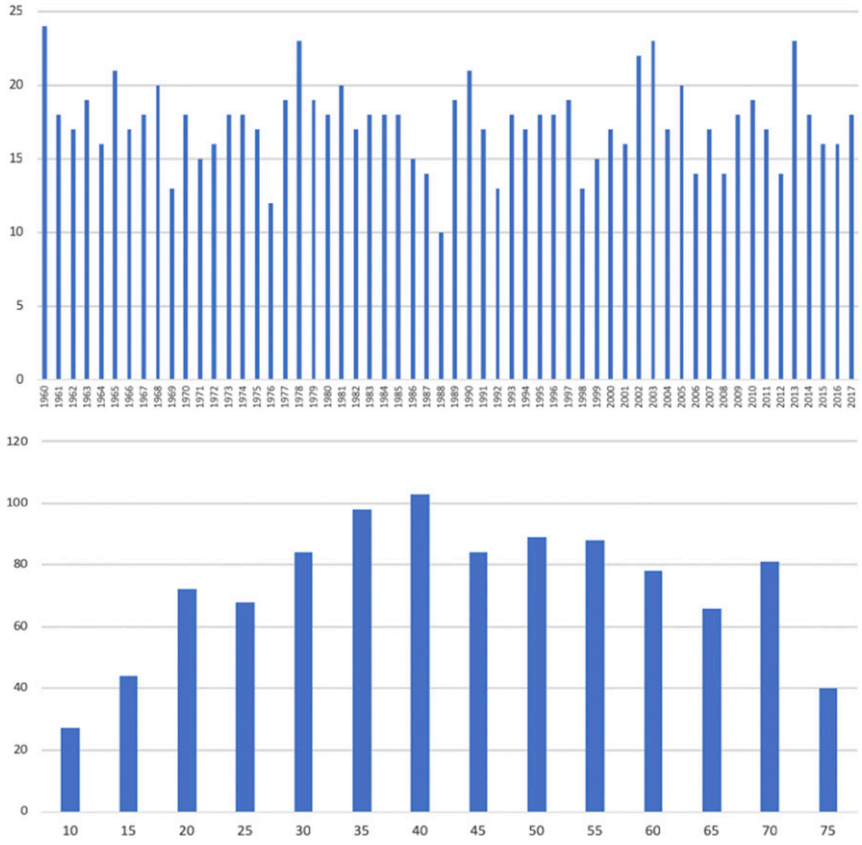

FIG. 2. Histogram of the total number of anticyclonic RWB events detected at (top) 350 K each year and (bottom) over the whole climatology by longitude.

latitude × 50° longitude is set around the high-PV centroid. For reference, a composite of the overturning 350-K isentropic PV is laid over the variables in black contours.

Additionally, to visualize the time evolution of anticyclonic RWB events, composite analyses are presented in a time series spanning from $T - 96$ to $T + 48$ h relative to the anticyclonic RWB event. Time-series composites are plotted over a larger domain, covering −20° to 40° latitude and −100° to 40° longitude around the high-PV centroid, allowing for upstream analysis of variables and processes. Composites of the 350-K isentropic PV are plotted over the variables in black contours at each time step as well. To also gain a better understanding of the vertical distribution of anticyclonic RWB environmental impacts, centroid-relative vertical cross-sectional composites are constructed by longitudinally averaging variables 2.5° around the centroid meridian over a −30° to 30° latitude domain.

3. Climatology

a. *Full basin*

A total of 1013 anticyclonic RWB events were detected over the North Atlantic basin during the summer from 1960 to 2017. The yearly distribution of the total number of events is shown in the top panel of Fig. 2. Throughout the climatology, between 17 and 18 anticyclonic RWB events were detected each year on average; however, the most active and inactive years were found to have as many as 20–24 events and as few as 10–13 events, respectively. This interannual frequency of anticyclonic RWB compares well with those presented in Postel and Hitchman (1999), Abatzoglou and Magnusdottir (2006), and Hitchman and Huesmann (2007). Expressed in number of PV reversals per 100 days (rpc), Hitchman and Huesmann (2007) observed between 20 and 40 rpc in the subtropics at 350 K for the months of June–August, whereas in the present study only 8–20 rpc, about half as many, were observed in the same region. While this may seem inconsistent, it must be noted that Hitchman and Huesmann (2007) used a much more relaxed latitudinal PV gradient of $\partial \mathrm{PV}/\partial y < 0$ versus the $\partial \mathrm{PV}/\partial y < -1.5$ threshold in this study. Additionally, their time counting was based on RWB days, not individual RWB events, which typically last for 2–3 days, accounting for the factor of 2–3 discrepancy observed in rpc between the two climatologies. Therefore, the climatology developed in

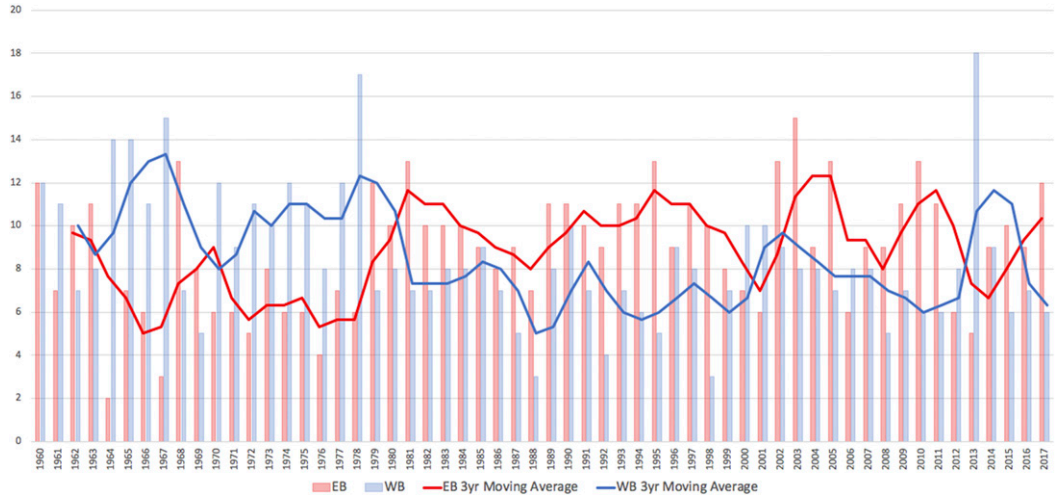

FIG. 3. Total number of EB and WB events per year (histogram) overlaid with a 3-yr moving average (line graph). Data for EB and WB events are displayed in red and blue, respectively.

Hitchman and Huesmann (2007) reasonably contains a greater total number of identified events and thus a higher rpc for the same region compared to that of the current study.

In Abatzoglou and Magnusdottir (2006), a larger latitudinal PV gradient threshold of $\partial \mathrm{PV}/\partial y < -2$ is utilized to identify anticyclonic RWB events over a 46-yr period, resulting in a significantly reduced frequency of identified events, about 225, over the North Atlantic from June to September. On the other hand, the latitudinal PV gradient threshold used in Postel and Hitchman (1999) is slightly smaller, such that $\partial \mathrm{PV}/\partial y < -1$. With this threshold, they identified a total of approximately 320 anticyclonic RWB events over the course of 10 years for the months of June–August. These results indicate that when using the stronger threshold of Abatzoglou and Magnusdottir (2006), an average frequency of approximately 5 events are recorded from June to September for each year, while the weaker threshold of Postel and Hitchman (1999) yields an average frequency of around 43 events. Given that this study uses a latitudinal PV gradient threshold that falls in between those of Abatzoglou and Magnusdottir (2006) and Postel and Hitchman (1999), it is logical that the average June–September frequency of anticyclonic RWB events for each year also falls in between those of the two studies.

When considering the monthly distribution of anticyclonic RWB events, consistent with Postel and Hitchman (1999) and Abatzoglou and Magnusdottir (2006), a slight majority of events (about 26%) were found to occur during the month of July (not shown). Additionally, in agreement with the results of Abatzoglou and Magnusdottir (2006), Martius et al. (2007), and Strong and Magnusdottir (2008), the longitudinal distribution of events across the basin (Fig. 2; bottom) reveals that anticyclonic RWB events over the North Atlantic occur most frequently in the central eastern region, with primary and secondary peaks in activity located around 40° and 70°W, respectively.

b. *Eastern and western basins*

Of the 1013 anticyclonic RWB events identified, 518 were classified as EB events while the remaining 495 were classified as WB events, a distribution consistent with the longitudinal spread observed in the bottom panel of Fig. 2. Though the similarity in the total number of EB and WB events over the 58-yr climatology might suggest a similar temporal distribution between the subgroups, further analysis of their interannual frequencies (Fig. 3) reveals very different characteristics. As shown in Fig. 3, the first 19 years of the climatology exhibits a favorability for WB over EB events, while the majority of the remaining 39 years of the climatology leans toward EB favorability. During the WB-favorability period, an average of 11 WB and 7 EB events were recorded each year. Conversely, an average of 7 WB and 10 EB events were recorded each year, virtually a complete reversal, during the EB-favorability period. Why such a variability between WB and EB events exists is unclear and prompts further investigation and is discussed in section 5.

4. Temporal and spatial characteristics

a. *Full basin*

Centroid-relative composites of the 200-hPa zonal and meridional wind anomalies surrounding all anticyclonic RWB events are exhibited in Figs. 4a and 4b. Both sets of anomalies clearly show anticyclonic circulation

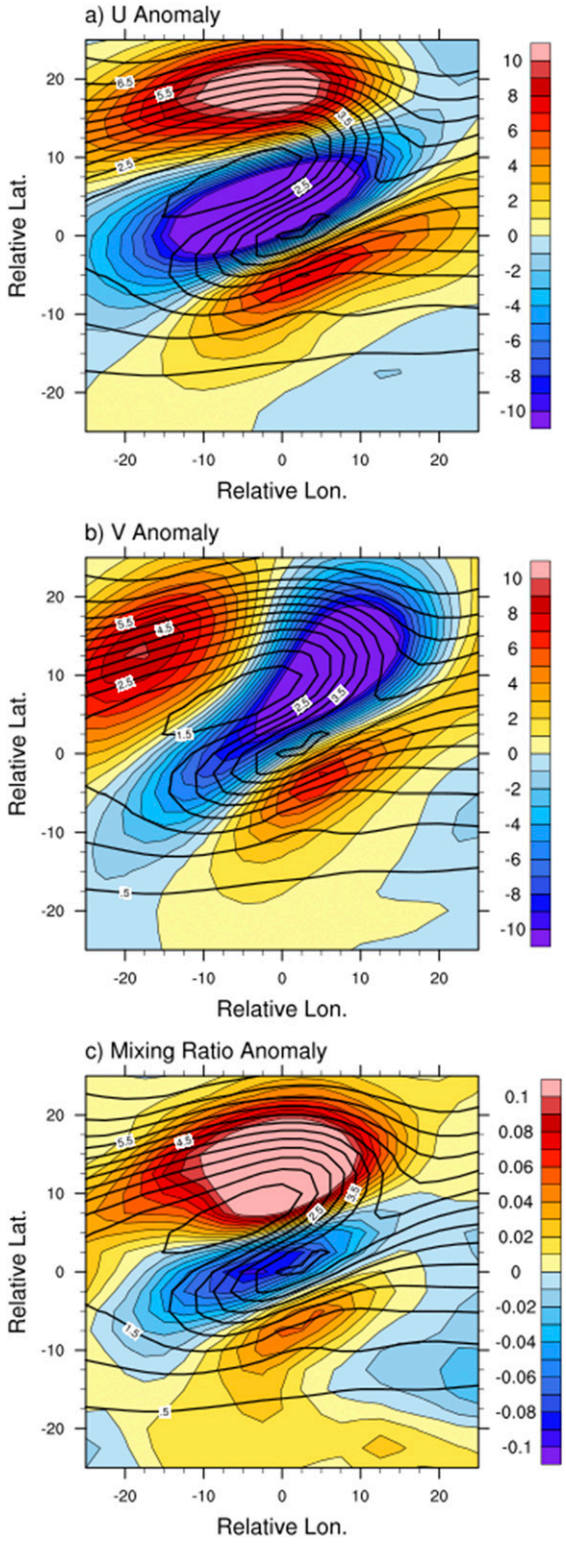

FIG. 4. Centroid-relative composites of 200-hPa (a) zonal and (b) meridional wind anomalies (shaded according to color bar; m s^{-1}) and (c) 300-hPa mixing ratio anomaly (shaded according to color bar; g kg^{-1}) for all anticyclonic RWB events. Black contours show the corresponding composite values of 350-K isentropic PV (PVU).

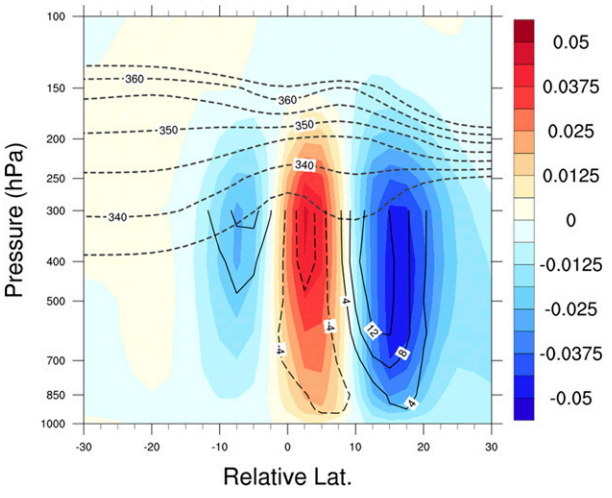

FIG. 5. Centroid-relative vertical cross-section composite of RH (contours; %) and VV (shaded according to color bar; Pa s^{-1}) anomalies for all anticyclonic RWB events. Dashed gray contours denote the composite vertical potential temperature profile from 335 to 365 K.

and cyclonic circulation to the northwest and southwest of the centroid, respectively, as well as a strongly reversed latitudinal PV gradient. This arrangement lends itself to equatorward transport of dry, stable stratospheric air along the high-PV tongue into the tropics and poleward transport of moist, unstable tropospheric air to the northwest of the high-PV tongue into the extratropics (Waugh and Polvani 2000), as evinced by the 300-hPa mixing ratio anomaly presented in Fig. 4c. The 300-hPa surface is used to visualize the mixing ratio because of the constraints of the NCEP–NCAR reanalysis dataset, in which data for the relative humidity, used in the calculation of the mixing ratio, is only available up to 300 hPa. Though not at 200 hPa, the mixing ratio anomaly at 300 hPa is still useful for providing insight into the upper troposphere–lower stratosphere moisture exchange associated with anticyclonic RWB. Additionally, the meridional wind anomalies in Fig. 4b display a northwest–southeast tilt of the breaking Rossby wave, indicative of equatorward energy dispersion and a poleward flux of westerly eddy momentum (Liebmann and Hartmann 1984; Kiladis and Weickmann 1992; Kiladis 1998).

Analysis of the centroid-relative vertical cross-sectional composite of relative humidity (RH) and vertical velocity (VV) anomalies (Fig. 5) provides insight into the vertical distribution of anticyclonic RWB's effect on the synoptic environment. This is important to visualize because the effects of RWB on the environment are not horizontally confined, as noted in previous studies relating RWB to changes in dynamical ozone distribution between the stratosphere and troposphere (Leovy et al. 1985; Holton et al. 1995; Leclair de Bellevue et al. 2006; Clain et al. 2010;

Hitchman and Rogal 2010). In this figure, the high-PV tongue is represented by a tightening of the vertical potential temperature gradient in lieu of PV itself. This relationship can be seen in the definition of PV given by Ertel (1942):

$$\mathrm{PV} = (\xi + f)\left(-g\frac{\partial\theta}{\partial p}\right), \tag{1}$$

such that PV is proportional to the vertical gradient of potential temperature θ and that changes in static stability often occur in phase with changes in total vorticity. Analysis of the composite reveals that, consistent with Waugh (2005), below and up to 10° north of the high-PV tongue, there is an increase in subsidence collocated with a strong reduction in RH. Both anomalies peak around 400–300 hPa and extend down to the surface, suggesting that the anticyclonic RWB high-PV tongue, with its dry and stable stratospheric air, produces an unfavorable environment for the maintenance and/or development of convection throughout the troposphere. Conversely, between 10° and 20° north of the high-PV tongue, RH and upward VV undergo a significant increase that also peaks around 400–300 hPa and extends down to the surface. However, unlike the previous pair, the maximum VV anomaly is displaced approximately 2° northward of the maximum RH anomaly. In this region, the poleward intrusion of moist, unstable tropical air facilitates a favorable environment for convection. A secondary, weaker region of enhanced RH and upward VV isolated to the midlevels can also be found approximately 10° to the south of the high-PV centroid.

A centroid-relative composite times series of 200-hPa meridional wind anomalies is shown for $T - 96$ to $T + 48$ h relative to all anticyclonic RWB events at 24-h intervals, shortened to 12-h intervals between $T - 24$ and $T + 24$ h (Fig. 6). At $T - 96$ h (Fig. 6a), there is only a faint indication of an upstream Rossby wave train (RWT) and ambient PV contours are relatively flat, save for a slight bump between −40° and −20° relative to the centroid. The observed weakness of this signal (and of that in Fig. 6b) is caused by the compositing process, as RWT development varies greatly among the 1013 individual events, especially between EB and WB members (as seen in Figs. 8a,c). Because of the overarching differences between the two subgroups as well as among all the individual members, compositing results in the differing signals being ''canceled out,'' leaving behind a small, virtually negligible signal. By $T - 72$ h (Fig. 6b), a slightly more robust upstream RWT signal begins to take form and is locked into place by the weak time-mean zonal winds of the North Atlantic subtropical surf zone (not shown; Postel and Hitchman 1999, 2001; Peters and Waugh 1996; Scott and Cammas 2002), organizing itself fully by $T - 48$ h (Fig. 6c). At this time, the anomalous meridional wind also begins to cause a shift in the ambient PV, reducing it upstream of the centroid in the region of anticyclonic circulation and increasing it near the centroid in the region of cyclonic circulation, simultaneously causing a tightening of the latitudinal PV contours in both regions. Over the next 24 h, the RWT piles up as energy propagates through the system, amplifying the downstream components, facilitating stronger meridional wind anomalies, and further tightening the PV contours. At this time, the high-PV tongue also begins to take shape as the RWT and associated meridional wind anomaly field take on a northwest–southeast tilt.

Around $T - 12$ h (Fig. 6e), a noticeable split in the downstream portion of the RWT can be observed, which becomes more pronounced over time until a complete split occurs at approximately $T + 12$ h (Fig. 6g). Additionally, at this time, the RWT has undergone a further tilt, such that the northerly meridional wind component has become northeasterly and the southerly meridional wind components have become southwesterly. This change in the meridional winds pushes the high-PV tongue out to the southwest, maximizing the latitudinal PV gradient reversal at $T + 0$ h (Fig. 6f). As strong mixing and energy dispersion through the end of the RWT occur over the next 24 h, the meridional wind anomalies weaken and, as a result, so do the anomalously high- and low-PV regions surrounding the centroid (Figs. 6g,h). At $T + 48$ h (Fig. 6i) the RWT has completely dispersed and, without the anomalous circulation patterns that accompany it, the ambient PV contours have begun to settle back into their normal, flat state.

b. *Eastern and western basins*

Centroid-relative vertical cross-section composites of RH and VV anomalies were also calculated for the EB and WB subgroups (Figs. 7a,b). Spatial distributions of the RH and VV anomalies for both subgroups bear a strong resemblance to the overall anticyclonic RWB composite (Fig. 5), but differences between them are easily discernible. Most notable is the presence of stronger negative anomaly signals for both fields in the WB composite versus the EB composite. Difference plots presented in Figs. 7c and 7d indicate that negative midlevel VV and RH anomalies for WB events are up to 1.5 and 2 times as large as those of their EB counterparts, respectively. Performing the Student's t test on these differences indicate that they are statistically significant at the 95% confidence level. The much more prevalent negative RH and VV anomalies present in WB events indicate that individual WB events alter the surrounding environment to a greater extent than EB events. While this may partly be caused by entrainment of nearby

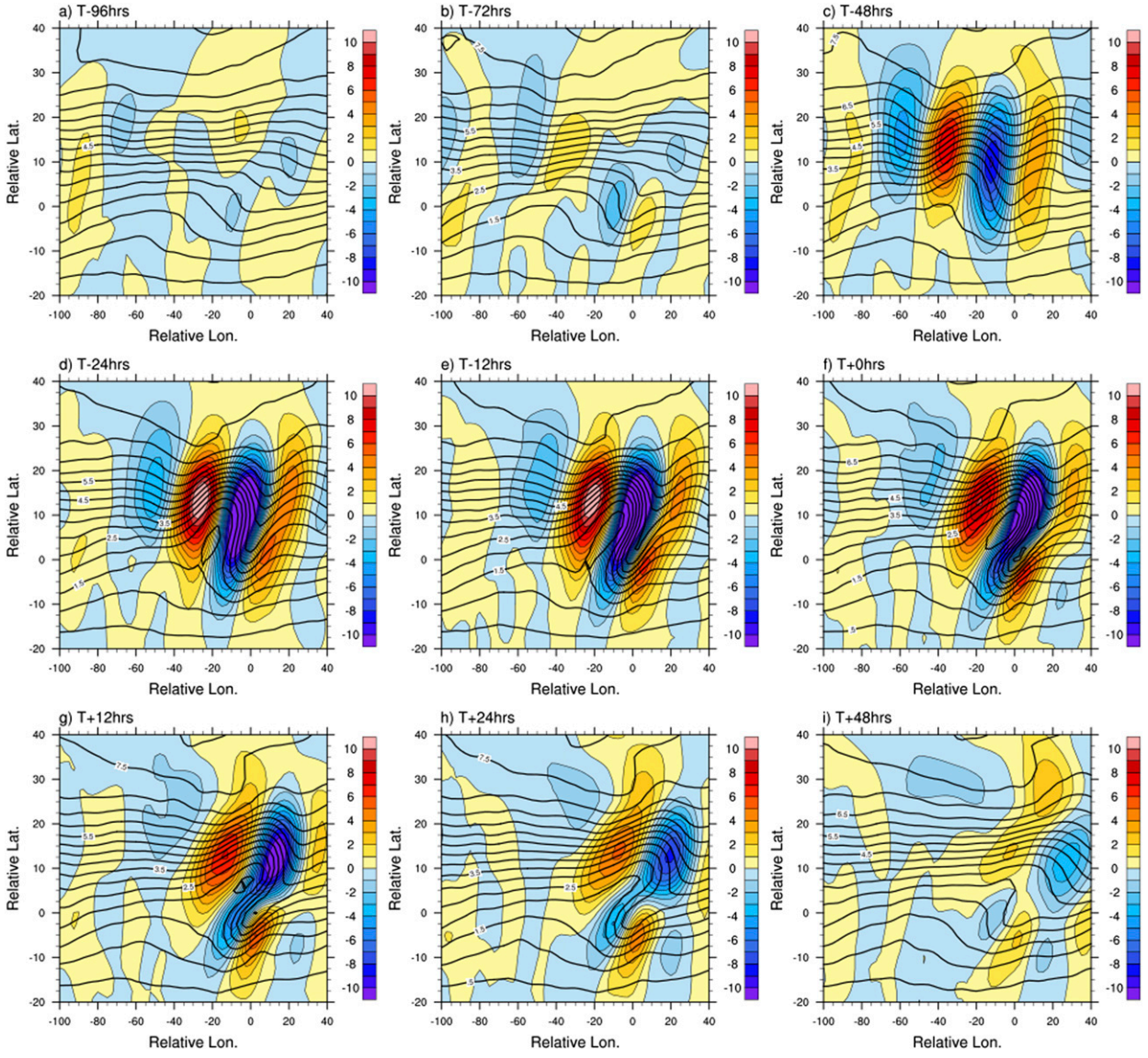

FIG. 6. Time-series evolution of 200-hPa meridional wind anomalies (shaded according to color bar; m s^{-1}) and 350-K isentropic PV (black contours; PVU) from (a) $T - 96$ to (i) $T + 48$ h relative to all anticyclonic RWB events at 24-h intervals, shortened to 12-h intervals between (d) $T - 24$ and (h) $T + 24$ h.

continental air, we believe, given the average longitude of WB events is 60°W and well away from the coast, that any such influence would be relatively small in the composites and not enough to create such a discrepancy between the two subgroups. These greater changes to the environment could explain why in Zhang et al. (2017) years with a higher frequency of WB events had a greater negative correlation with TC count than years with a higher frequency of EB events.

Further inspection of the composites reveals that not only is there a difference in anomaly strength but also anomaly location between the subgroups. WB events tend to have both sets of RH and VV anomaly maxima collocated, while EB events, in similarity to the full composite, exhibit a 5°–6° displacement between its northern RH and VV positive anomaly maxima. Furthermore, anomalies associated with WB events are more latitudinally confined than those of EB events, lying between 10°S and 20°N of the centroid with little space between the opposing maxima. On the other hand, EB anomaly maxima are spread much further apart, with the northern positive VV anomalies displaced approximately 2° north of their WB counterparts and reaching significantly past 20° north of the centroid. These structural discrepancies can be clearly observed from 10° to 30° north of the centroid in Figs. 7c and 7d. Minor variations

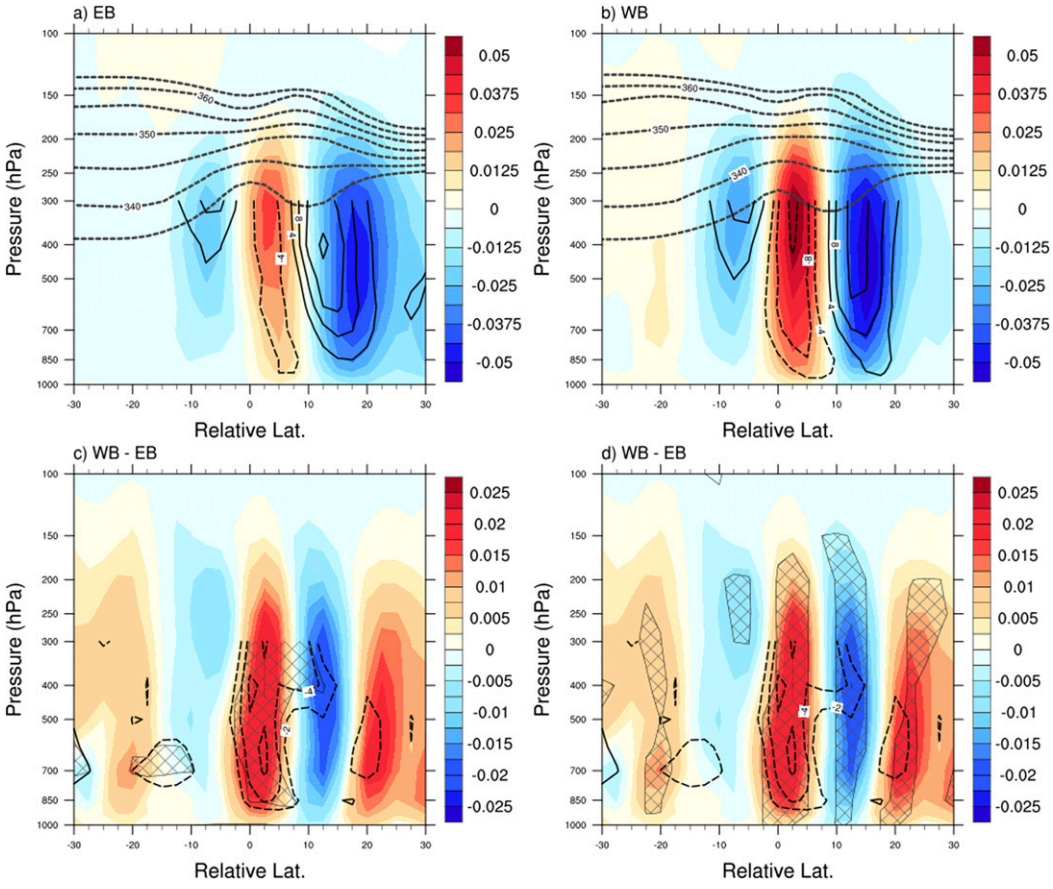

FIG. 7. As in Fig. 5, but for (a) EB events, (b) WB events, and (c),(d) their difference. Cross hatching in (c) and (d) indicate regions where RH and VV, respectively, are significantly different between (a) and (b) at the 95% confidence level.

in both the large-scale circulation patterns and associated high-PV tongues that exist between EB and WB events is the most likely explanation for the observed differences in synoptic environmental characteristics.

When split into the EB and WB subgroups, the time-series composites of the 200-hPa meridional wind anomalies for each reflect the same temporal and spatial evolutions as the total anticyclonic RWB time series. The primary difference between the subgroups is most clearly observed at $T - 96$ h and is related to the location of RWT initiation. Time-relative composites at $T - 96$ h of 200-hPa meridional wind anomalies for EB and WB events are presented in Figs. 8a and 8c, respectively. It is clear from a side-by-side comparison of these composites that, while EB RWTs appear to preferentially originate just off the western coast of the United States, WB RWTs have their origins much farther west in the western/central North Pacific. This discrepancy in RWT initiation location could explain the observed differences in synoptic environmental characteristics between EB and WB events. As in Figs. 7c and 7d, the Student's t test is performed on the difference between EB- and WB-event meridional wind anomalies at $T - 96$ h (Fig. 8e), revealing that the two observed RWTs are indeed statistically different at the 95% confidence level.

The evolution and propagation of the composite RWTs are summarized in Hovmöller diagrams of 40°–65°N and 35°–60°N latitudinally averaged 200-hPa meridional wind anomalies from $T - 144$ to $T + 48$ h relative to anticyclonic RWB for the EB and WB subgroups, respectively (Figs. 8b,d). Consistent with Figs. 8a and 8c, the Hovmöller diagrams clearly show a difference in the EB and WB subgroup RWT initialization longitudes. Following Joung and Hitchman (1982), the group velocities of the RWTs that precede the EB and WB events as well as the zonal phase speeds of individual components that make up the RWTs are calculated using the following formula:

$$c_x = \frac{a\cos(\overline{\phi})\Delta\overline{\lambda}}{\Delta t}, \tag{2}$$

where c_x is the zonal phase speed, $a = 6367$ km is the radius of Earth, $\overline{\phi}$ is the average latitude of the center of

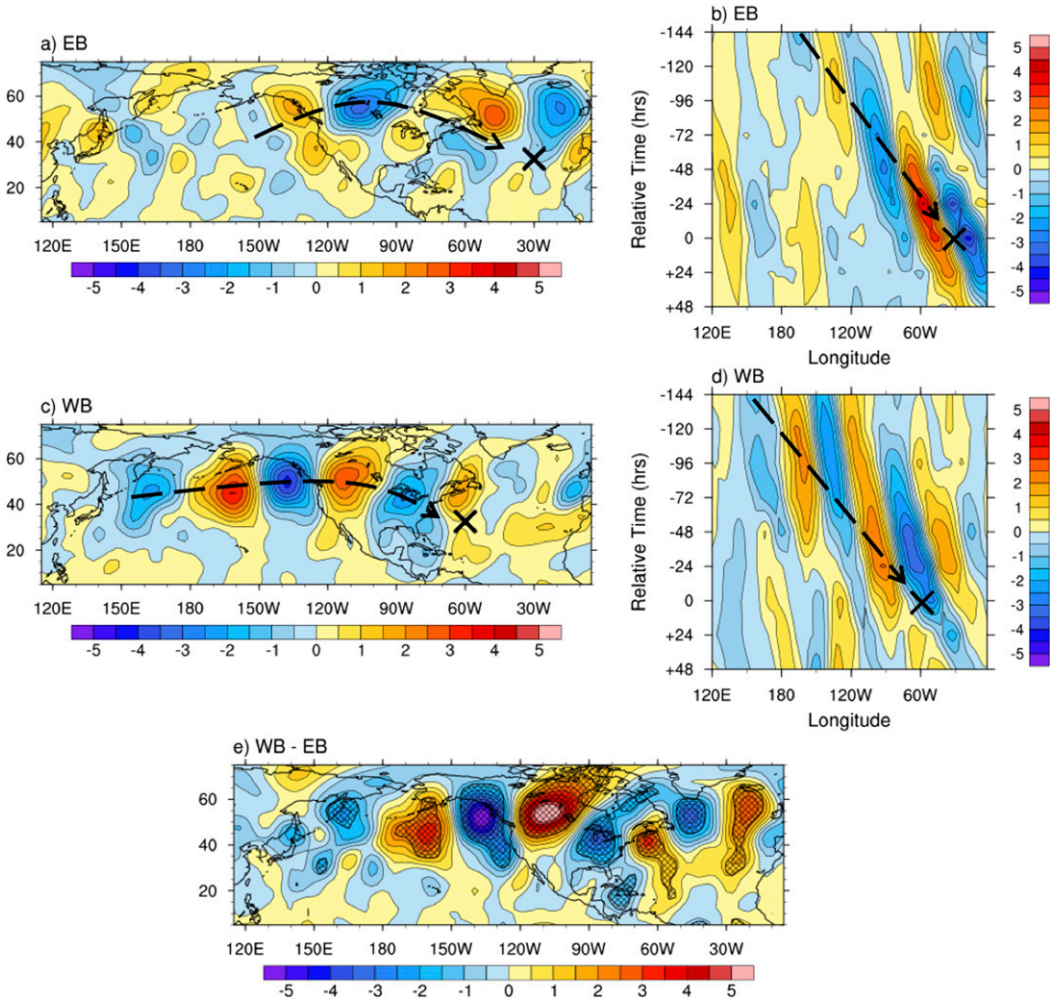

FIG. 8. Time-relative composites of 200-hPa meridional wind anomalies (shaded according to color bar; m s^{-1}) at $T - 96$ h for (a) EB events, (c) WB events, and (e) their difference. Composite Hovmöller diagrams of (b) 40°–65° and (d) 35°–60°N latitudinally averaged 200-hPa meridional wind anomalies (shaded according to color bar; m s^{-1}) from $T - 144$ to $T + 48$ h for EB and WB events, respectively. An × marks the average centroid location at $T + 0$ h for each respective subgroup, dashed lines in (a) and (c) denote the approximate downstream propagation and in (b) and (d) the group velocities of the precursor RWTs, and cross hatching in (e) indicates regions where (a) and (c) are significantly different at the 95% confidence level.

the wave train, and $\Delta\overline{\lambda}$ is the change in longitude of the average longitude center of the wave train, which corresponds to the location of the maximum amplitude. This formula is useful as it allows for the tracking of individual troughs and ridges by eye, giving an observed estimate for zonal phase speed c_x, while also providing a means to track the center of maximum wave amplitude, giving an estimate for zonal group speed G_x. In both sets of composites, the zonal phase speeds of the individual components range from 3.4 to 8.6 m s^{-1}, while the group velocities of the EB and WB RWTs are 17 and 21 m s^{-1}, respectively. Overall, these numbers are consistent with those found in Joung and Hitchman (1982) for a downstream-propagating RWT and Rossby wave theory, in which the group velocity of a RWT is greater than the phase speeds of the individual components that make up the RWT itself.

While the group velocities, and thus the energy-propagation speeds, of both RWTs are found to have similar magnitudes, the meridional wind anomalies in the EB RWT are much less robust than those in the WB RWT from $T - 144$ to $T - 48$ h. This difference may be due to the mechanism of RWT initialization being much weaker or displaced farther south for EB events than their WB counterparts, resulting in a much slower amplification of the RWT. A deeper investigation into the discrepancies between EB and WB RWT initialization location and strength is discussed in the next section.

TABLE 1. Correlation coefficients for the June–September-averaged PDO, NAM, multivariate ENSO, PNA, and NAO indices vs EB − WB frequency, EB frequency, WB frequency, the total number of events, and latitudinal variation.

	EB − WB	EB	WB	Total	Latitude
PDO	0.381	0.374	−0.301	0.043	0.091
NAM	−0.097	−0.134	0.042	0.089	0.208
MEI	0.275	0.241	−0.244	−0.028	−0.009
PNA	0.176	−0.100	−0.100	0.107	0.105
NAO	−0.380	−0.226	0.434	0.254	0.049

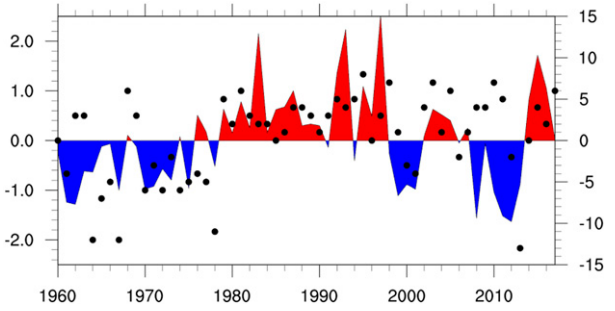

FIG. 9. Time series of the June–September-averaged PDO index from 1960 to 2017 (shaded; values on left axis) overlaid by the difference between EB and WB events for that given year (black dots; values on right axis).

5. Anticyclonic RWB modulation

To better understand what modulates the frequency and location of North Atlantic anticyclonic RWB events, the total and intrabasin distributions of the climatology were compared to high- and low-frequency extratropical and tropical teleconnection patterns. The correlation coefficients for the Pacific decadal oscillation (PDO), northern annular mode (NAM), multivariate ENSO (MEI), Pacific–North America teleconnection (PNA), and NAO indices averaged over the months of June–September versus EB minus WB frequency, EB frequency, WB frequency, the total number of events, and latitudinal variation, respectively, can be found in Table 1. As shown in the table, the only climate mode that has any correlation with the interannual variation in anticyclonic RWB frequency over the North Atlantic is the NAO. However, as discussed in Strong and Magnusdottir (2008), this relationship is most likely due to the NAO's response to anticyclonic RWB, such that, as shown in their Fig. 5a, a positive (negative) NAO is driven by an abundance of anticyclonic RWB in the subtropical western (eastern) North Atlantic, thus the correlation is likely driven by the anticyclonic RWB activity and not the NAO itself. In regards to the latitudinal variation of RWB events, the correlation coefficients are found to be relatively weak for all climate indices save for the NAM, which is shown to have a small, positive correlation. This relationship is likely because during a positive (negative) NAM, the subtropical jet stream has a tendency to be shifted poleward (equatorward; Thompson and Wallace 2000). Because anticyclonic RWB is favored on the equatorward side of the jet (Thorncroft et al. 1993; Abatzoglou and Magnusdottir 2006; Zhang et al. 2017), a poleward-shifted jet would thus lead to a poleward displacement of anticyclonic RWB.

While the NAM is found to have almost no correlation with EB versus WB favorability, both the PNA and ENSO are shown to have moderate correlations, though not as strong as those for the PDO and the NAO. As similarly noted for interannual variation in the previous paragraph, the NAO-related intrabasin frequency correlations are most likely due to the NAO's response to anticyclonic RWB activity over the North Atlantic and not the NAO's influence over the intrabasin RWB frequency. Therefore, when considering the intrabasin frequency of anticyclonic RWB events, the most meaningful correlation is found with the averaged PDO index. As shown in Fig. 9, when the averaged PDO index (Mantua and Hare 1997) is positive, there is a favorability for EB events, while the opposite holds true when the averaged PDO index is negative. Out of the 58-yr climatology, 40 years (69%) follow this relationship, 14 years (24%) do not, and 4 years (7%) displayed no favorability. Additionally, correlation coefficients are calculated for the averaged PDO index versus EB minus WB events, EB events only, and WB events only. Respectively, the coefficients are 0.38, 0.37, and −0.30.

As the leading principal component of North Pacific monthly sea surface temperature (SST) variability poleward of 20°N (Mantua et al. 1997; Zhang et al. 1997), the PDO plays a role in modulating North Pacific large-scale circulation patterns (Latif and Barnett 1996; Mantua et al. 1997; Gershunov and Barnett 1998; Nigam et al. 1999). When the PDO is in its positive phase, positive SST anomalies are present in the eastern North Pacific, extending from Mexico to the Gulf of Alaska, and negative SST anomalies are found in the western and central extratropical North Pacific. The opposite is true during the negative phase of the PDO. In the summertime, PDO-related circulation variability is caused by an upper-level atmospheric response to convective heating forced by anomalous SSTs. As a part of this response, large fluxes of stationary wave activity and anomalous upper-atmospheric ridges are built up, which serve to excite RWTs (Lau and Peno 1992; Kiladis and Weickmann 1997; Lau and Weng 2002). Driven by the enhanced horizontal wave activity, these RWTs then organize and propagate downstream, introducing anomalous circulation patterns over North America and the North Atlantic (Barlow et al. 2001).

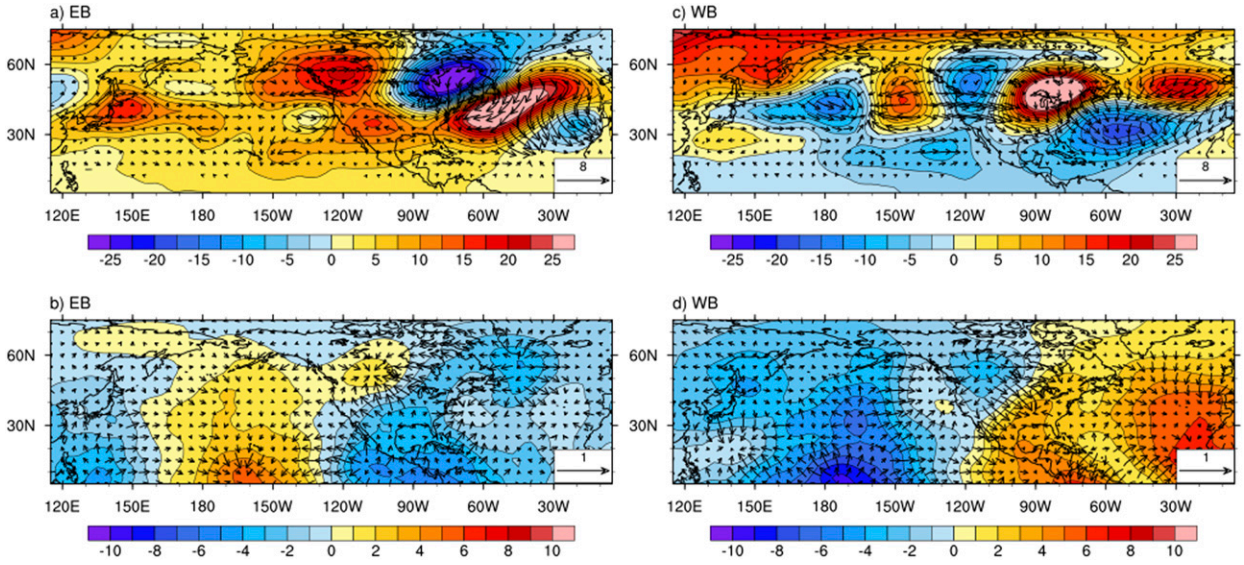

FIG. 10. (top) Horizontal stationary wave activity flux vectors (arrows; $m^2 s^{-2}$) and geopotential height anomalies (shaded according to color bar; gpm) at 200 hPa averaged from $T - 96$ to $T - 24$ h relative to anticyclonic RWB for (a) EB and (c) WB events. (bottom) Time-relative composites of 200-hPa velocity potential (scaled by 1×10^{-5}, shaded according to color bar; $m^2 s^{-1}$) and divergent wind (arrows; $m s^{-1}$) anomalies at $T - 96$ for (b) EB and (d) WB events.

To examine the connection between the PDO and anticyclonic RWB location frequency in more detail, analyses of the 200-hPa horizontal wave activity flux (Plumb 1985) and geopotential height anomalies composited from $T - 96$ to $T - 24$ h for all EB and WB events (Figs. 10a,c) as well as EB and WB events during both PDO+ and PDO− regimes are performed (Fig. 11). The composites show that for each subgroup, a localized atmospheric response is occurring in the form of a downstream-propagating RWT, as evinced by the direction of the horizontal wave activity fluxes. Analysis of both sets of composites in Fig. 11 reveals that the precursor RWTs associated with both EB and WB events tend to initialize farther north and east during PDO+ regimes than during PDO− regimes, suggesting that where the precursor RWTs originate is

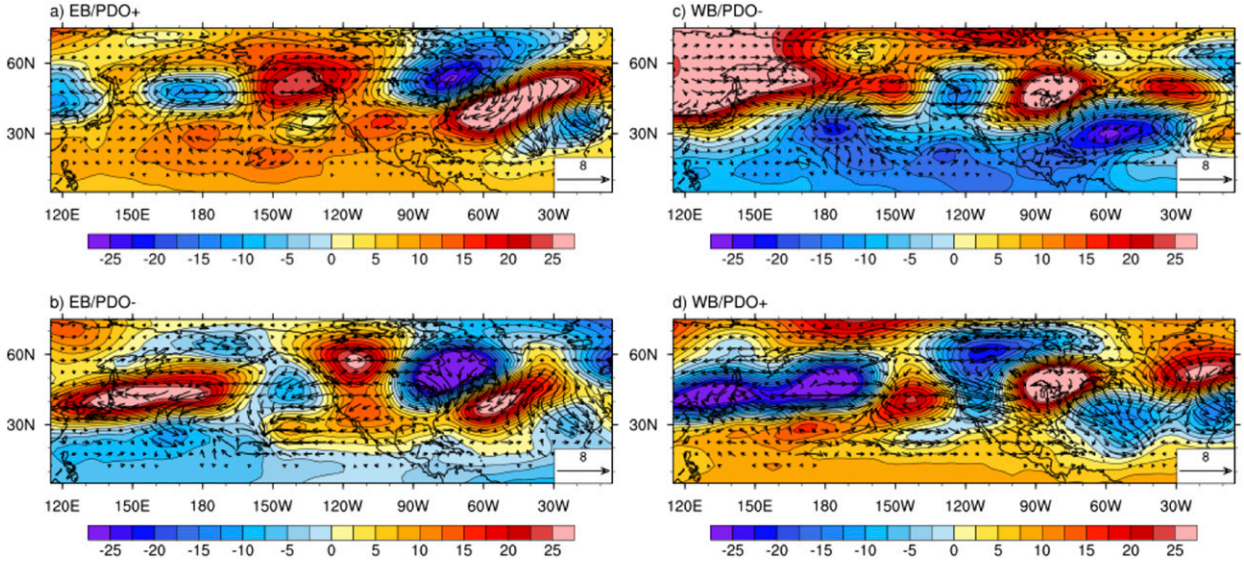

FIG. 11. As in Figs. 10a and 10c, but for (left) EB events that occurred during (a) PDO+ and (b) PDO− regimes and (right) WB events that occurred during (c) PDO− and (d) PDO+ regimes.

dictated by the phase of the PDO and its associated SST anomalies.

Closer examination of Figs. 11b and 11d reveals that EB and WB events during PDO− and PDO+ regimes, respectively, bear structurally similar, yet opposite in magnitude, RWT patterns that originate over the Kuroshio–Oyashio Extension (KOE) region. The two tripole, equivalent barotropic RWT patterns observed over the extratropical North Pacific strongly resemble those found in studies by Frankignoul and Sennéchael (2007) and O'Reilly and Czaja (2015), who both argue that decadal variations of summertime SST anomalies in the KOE region have a significant impact on midlatitude large-scale climate variability. This KOE-driven atmospheric response could thus explain why EB and WB events still occur during PDO− and PDO+ regimes, respectively. Worth noting, however, is that in the full composites (Figs. 10a,c), the majority of precursor RWTs associated with EB (WB) events originate over the eastern (western) Pacific, supporting the hypothesis that EB (WB) events are favored during PDO+ (PDO−) regimes.

Building on this hypothesis, one can argue that during PDO+ (PDO−) tropical convection, and by extension TC development, is more suppressed in the eastern (western) North Atlantic because of the higher frequency of anticyclonic RWB occurring there. As mentioned in the previous section, anticyclonic RWB is associated with the introduction of anomalously dry and stable extratropical air into the tropical environment, which serves to inhibit convection. Given this relationship, when there is an increase in the frequency of anticyclonic RWB in the eastern North Atlantic, fewer TCs are likely to develop there than in the western North Atlantic, where the environment is considerably more favorable. Therefore, this suggests that when the PDO is in its positive phase, driving an increase in the frequency of convection-inhibiting EB events, TC development will be favored in the western North Atlantic and vice versa. As such, this three-pronged connection among PDO phase, intrabasin anticyclonic RWB modulation, and TC development could prove useful in North Atlantic tropical cyclogenesis forecasting.

To further investigate how convective heating and RWT excitement are related, time-relative composites of precipitation rate anomalies (not shown) and 200-hPa velocity potential and divergent wind anomalies at $T - 96$ h for all EB and WB events are calculated (Figs. 10b,d). Both of the composites exhibit regions of anomalously high precipitation rate, low velocity potential, and divergent outflow that are longitudinally collocated with the initialized RWT for each subgroup. These anomaly patterns suggest that outflow from anomalous convection driven by positive SST anomalies can possibly contribute to the buildup of the upper-atmospheric ridge that excites the precursor RWTs (Hoskins and Karoly 1981; Lau and Peno 1992; Kiladis and Weickmann 1997; Higgins and Mo 1997; Higgins et al. 2000; Lau and Weng 2002). The meridional locations of these anomalies could also help explain, as mentioned earlier, why the EB meridional wind anomalies from $T - 144$ to $T - 48$ h are much weaker than the WB meridional wind anomalies. A side-by-side comparison of Figs. 10b and 10d show that the EB velocity potential and divergent wind anomalies are weaker and located 10°–15° farther south than the WB anomalies. This means that there is less convective outflow feeding into a more northerly displaced atmospheric circulation response in EB events than WB events, thus generating a weaker initial response that amplifies over time.

Despite undergoing similar temporal evolutions, as shown in section 4b, the precursor RWTs related to EB events preferentially originate farther to the east than those related to WB events (Figs. 10a,c). This can be attributed to the differing spatial distribution of positive SST anomalies between PDO+ and PDO− regimes modulating the location of anomalous convective heating, thus dictating where the initial ridge of the precursor RWTs and buildup of stationary wave activity flux occurs. It is logical to assume that because PDO+ SST anomalies are located farther east the RWTs that originate there, the majority of which are associated with EB events, complete their great-circle routes (Hoskins et al. 1977), interact with the North Atlantic subtropical surf zone, and break farther east than the RWTs that originate over the positive SST anomalies associated with PDO−. Therefore, during PDO+ regimes, there is a preference for EB events and vice versa.

6. Summary and discussion

This study develops a climatology and analyzes the synoptic environmental impacts surrounding North Atlantic summertime anticyclonic RWB events using 58 years of NCEP–NCAR reanalysis data. Anticyclonic RWB events are identified on the 350-K isentropic surface using an objective, three-criteria algorithm and then further examined to ensure the fulfillment of additional spatial and temporal requirements. A total of 1013 anticyclonic RWB events were detected and found to occur most frequently in the middle of the basin, with primary and secondary peaks in activity located around 40° and 70°W, respectively. While the intrabasin climatology reveals that the total number of EB and WB events throughout the climatology are very similar, there is a multidecadal pattern of higher frequency of occurrence of one subgroup over another.

High-PV-tongue centroid-relative composites show that during an anticyclonic RWB event, anticyclonic

circulation to the northwest and cyclonic circulation to the southwest of the centroid allow for equatorward transport of dry, stable stratospheric air along the high-PV tongue into the tropics and poleward transport of moist, unstable tropospheric air to the northwest of the high-PV tongue into the extratropics. Additionally, the centroid-relative vertical cross-sectional composite of RH and VV anomalies show that under the anticyclonic RWB high-PV tongue, the intrusion of dry and stable air produces an unfavorable environment for the maintenance and/or development of convection. Conversely, to the north of the high-PV tongue, the poleward intrusion of moist, unstable tropical air facilitates a favorable environment for convection. The same centroid-relative composites were made for both the EB and the WB subgroups. Spatial distributions of the RH and VV anomalies for both subgroups bear a strong resemblance to the overall anticyclonic RWB composite, but the negative midlevel VV and RH anomalies for WB events are up to 1.5 and 2 times, respectively, as large as those of their EB counterparts. Additionally, time-relative composites at $T - 96$ h of 200-hPa meridional wind anomalies for each subgroup show that EB RWTs appear to preferentially originate just off the western coast of the United States, while WB RWTs have their origins much farther west in the western/central North Pacific.

To ascertain what modulates the frequency and location of North Atlantic anticyclonic RWB events, the total and intrabasin distributions of the climatology were compared to high- and low-frequency extratropical and tropical teleconnection patterns. A potentially meaningful correlation between the intrabasin distribution of anticyclonic RWB events and the June–September-averaged PDO index was found, such that when the PDO is positive, there is a favorability for EB events, while the opposite holds true when the averaged PDO index is negative. In an effort to understand the connection between the intrabasin distribution of anticyclonic RWB events and the June–September-averaged PDO index, analyses of 1) the 200-hPa horizontal wave activity flux and geopotential height anomalies composited from $T - 96$ to $T - 24$ h and 2) the time-relative composite of 200-hPa velocity potential and divergent wind anomalies at $T - 96$ h for all EB and WB events as well as EB and WB events during both PDO+ and PDO− regimes are performed. The composites show that, as suggested in previous studies, convectively forced atmospheric responses to PDO-related positive SST anomalies excite RWTs that propagate downstream and break over the North Atlantic. The differing distribution of positive SST anomalies between PDO+ and PDO− regimes, therefore, modulates how far east or west the initial ridge building occurs, the precursor RWTs form, their propagation paths, and where they ultimately break. The total EB- and WB-event composites shown in Figs. 10a and 10c suggest that the majority of RWTs associated with EB (WB) events originate over the eastern (western) Pacific, supporting the hypothesis that EB (WB) events are favored during PDO+ (PDO−) regimes. However, in order to determine whether or not the PDO does, in fact, play a primary role in modulating the intrabasin distribution of anticyclonic RWB, a modeling study will be employed, the results of which will be presented in a future paper.

While the argument for the connection between the PDO and intrabasin frequency and location of anticyclonic RWB events holds for a majority of the climatology, a glaring contradiction to that connection exists between 2008 and 2011 (Fig. 9). Despite a persistently strong negative PDO, a significant preference for EB events over WB events is recorded for those years. While it is unclear why the observations contradict what is expected, one possible explanation, mentioned in the previous section, is that it could be attributed to the decadal variability of the KOE's SST anomalies in the extreme western half of the PDO signal (Latif and Barnett 1994, 1996; Qiu 2003; Schneider and Cornuelle 2005). As seen in Fig. 11b, during the PDO− regime, EB-event RWTs tend to develop farther west than WB-event RWTs, right over the region where the KOE has maximum influence over SSTs. Frankignoul and Sennéchael (2007) and O'Reilly and Czaja (2015) both noted that a positive SST anomaly in the KOE region forces a RWT pattern reminiscent of that observed for EB events during PDO−, suggesting that very strong positive SST anomalies in the KOE could drive the development of a greater number of RWTs associated with the EB events than WB events even if the PDO is in a negative regime and vice versa. When considering the time period from 2008 to 2011, the Kuroshio Extension induced large positive SST anomalies over the extreme western Pacific for 3 of the 4 years, potentially leading to the initiation of a greater number of RWTs favorable for EB RWB and contributing, in part, to the discrepancy observed in Fig. 9. The Kuroshio Extension's role in producing SST anomalies, forcing RWTs, and stationary wave activity production will need to be further investigated to test this hypothesis.

Acknowledgments. The authors thank the National Oceanic and Atmospheric Administration for their support under Grants NA160AR4310141, NA160AR4310149, and NA150AR4320064. We would also like to acknowledge the two anonymous reviewers for their constructive comments and valuable suggestions, the University of Miami Center for Computational Science for providing indispensable computational resources, and the NCAR Research Data Archive for access to the NCEP–NCAR reanalysis dataset.

REFERENCES

Abatzoglou, J. T., and G. Magnusdottir, 2006: Planetary wave breaking and nonlinear reflection: Seasonal cycle and interannual variability. *J. Climate*, **19**, 6139–6152, https://doi.org/10.1175/JCLI3968.1.

Allen, G., G. Vaughan, D. Brunner, P. T. May, W. Heyes, P. Minnis, and J. K. Ayers, 2009: Modulation of tropical convection by breaking Rossby waves. *Quart. J. Roy. Meteor. Soc.*, **135**, 125–137, https://doi.org/10.1002/qj.349.

Barlow, M., S. Nigam, and E. H. Berbery, 2001: ENSO, Pacific decadal variability, and US summertime precipitation, drought, and stream flow. *J. Climate*, **14**, 2105–2128, https://doi.org/10.1175/1520-0442(2001)014<2105:EPDVAU>2.0.CO;2.

Benedict, J. J., S. Lee, and S. B. Feldstein, 2004: Synoptic view of the North Atlantic Oscillation. *J. Atmos. Sci.*, **61**, 121–144, https://doi.org/10.1175/1520-0469(2004)061<0121:SVOTNA>2.0.CO;2.

Clain, G., J.-L. Baray, R. Delmas, P. Keckhut, and J.-P. Cammas, 2010: A Lagrangian approach to analyse the tropospheric ozone climatology in the tropics: Climatology of stratosphere–troposphere exchange at Reunion Island. *Atmos. Environ.*, **44**, 968–975, https://doi.org/10.1016/j.atmosenv.2009.08.048.

Ertel, H., 1942: Ein neuer hydrodynamischer Wirbelsatz. *Meteor. Z.*, **59**, 277–281.

Frankignoul, C., and N. Sennéchael, 2007: Observed influence of North Pacific SST anomalies on the atmospheric circulation. *J. Climate*, **20**, 592–606, https://doi.org/10.1175/JCLI4021.1.

Franzke, C., S. Lee, and S. B. Feldstein, 2004: Is the North Atlantic Oscillation a breaking wave? *J. Atmos. Sci.*, **61**, 145–160, https://doi.org/10.1175/1520-0469(2004)061<0145:ITNAOA>2.0.CO;2.

Gabriel, A., and D. Peters, 2008: A diagnostic study of different types of Rossby wave breaking events in the northern extratropics. *J. Meteor. Soc. Japan*, **86**, 613–631, https://doi.org/10.2151/jmsj.86.613.

Gershunov, A., and T. P. Barnett, 1998: Interdecadal modulation of ENSO teleconnections. *Bull. Amer. Meteor. Soc.*, **79**, 2715–2725, https://doi.org/10.1175/1520-0477(1998)079<2715:IMOET>2.0.CO;2.

Higgins, R. W., and K. C. Mo, 1997: Persistent North Pacific circulation anomalies and the tropical intraseasonal oscillation. *J. Climate*, **10**, 223–244, https://doi.org/10.1175/1520-0442(1997)010<0223:PNPCAA>2.0.CO;2.

——, J.-K. E. Schemm, W. Shi, and A. Leetmaa, 2000: Extreme precipitation events in the western United States related to tropical forcing. *J. Climate*, **13**, 793–820, https://doi.org/10.1175/1520-0442(2000)013<0793:EPEITW>2.0.CO;2.

Hitchman, M. H., and A. S. Huesmann, 2007: A seasonal climatology of Rossby wave breaking in the 320–2000-K layer. *J. Atmos. Sci.*, **64**, 1922–1940, https://doi.org/10.1175/JAS3927.1.

——, and M. J. Rogal, 2010: Influence of tropical convection on the Southern Hemisphere ozone maximum during the winter to spring transition. *J. Geophys. Res.*, **115**, D14118, https://doi.org/10.1029/2009JD012883.

Holton, J. R., P. H. Haynes, M. E. McIntyre, A. R. Douglass, R. B. Rood, and L. Pfister, 1995: Stratosphere-troposphere exchange. *Rev. Geophys.*, **33**, 403–439, https://doi.org/10.1029/95RG02097.

Hoskins, B. J., and D. J. Karoly, 1981: The steady linear response of a spherical atmosphere to thermal and orographic forcing. *J. Atmos. Sci.*, **38**, 1179–1196, https://doi.org/10.1175/1520-0469(1981)038<1179:TSLROA>2.0.CO;2.

——, A. J. Simmons, and D. G. Andrews, 1977: Energy dispersion in a barotropic atmosphere. *Quart. J. Roy. Meteor. Soc.*, **103**, 553–567, https://doi.org/10.1002/qj.49710343802.

——, M. E. McIntyre, and A. W. Robertson, 1985: On the use and significance of isentropic potential vorticity maps. *Quart. J. Roy. Meteor. Soc.*, **111**, 877–946, https://doi.org/10.1002/qj.49711147002.

Joung, C. H., and M. H. Hitchman, 1982: On the role of successive downstream development in East Asian polar air outbreaks. *Mon. Wea. Rev.*, **110**, 1224–1237, https://doi.org/10.1175/1520-0493(1982)110<1224:OTROSD>2.0.CO;2.

Kalnay, E., and Coauthors, 1996: The NCEP/NCAR 40-Year Reanalysis Project. *Bull. Amer. Meteor. Soc.*, **77**, 437–471, https://doi.org/10.1175/1520-0477(1996)077<0437:TNYRP>2.0.CO;2.

Kiladis, G. N., 1998: Observations of Rossby waves linked to convection over the eastern tropical Pacific. *J. Atmos. Sci.*, **55**, 321–339, https://doi.org/10.1175/1520-0469(1998)055<0321:OORWLT>2.0.CO;2.

——, and K. M. Weickmann, 1992: Extratropical forcing of tropical Pacific convection during northern winter. *Mon. Wea. Rev.*, **120**, 1924–1939, https://doi.org/10.1175/1520-0493(1992)120<1924:EFOTPC>2.0.CO;2.

——, and ——, 1997: Horizontal structure and seasonality of large-scale circulations associated with submonthly tropical convection. *Mon. Wea. Rev.*, **125**, 1997–2013, https://doi.org/10.1175/1520-0493(1997)125<1997:HSASOL>2.0.CO;2.

Knippertz, P., 2007: Tropical–extratropical interactions related to upper-level troughs at low latitudes. *Dyn. Atmos. Oceans*, **43**, 36–62, https://doi.org/10.1016/j.dynatmoce.2006.06.003.

Latif, M., and T. P. Barnett, 1994: Causes of decadal climate variability over the North Pacific and North America. *Science*, **266**, 634–637, https://doi.org/10.1126/science.266.5185.634.

——, and ——, 1996: Decadal climate variability over the North Pacific and North America: Dynamics and predictability. *J. Climate*, **9**, 2407–2423, https://doi.org/10.1175/1520-0442(1996)009<2407:DCVOTN>2.0.CO;2.

Lau, K.-M., and L. Peno, 1992: Dynamics of atmospheric teleconnections during the northern summer. *J. Climate*, **5**, 140–158, https://doi.org/10.1175/1520-0442(1992)005<0140:DOATDT>2.0.CO;2.

——, and H. Weng, 2002: Recurrent teleconnection patterns linking summertime precipitation variability over East Asia and North America. *J. Meteor. Soc. Japan*, **80**, 1309–1324, https://doi.org/10.2151/jmsj.80.1309.

Leclair de Bellevue, J., A. Réchou, J. L. Baray, G. Ancellet, and R. D. Diab, 2006: Signatures of stratosphere to troposphere transport near deep convective events in the southern subtropics. *J. Geophys. Res.*, **111**, D24107, https://doi.org/10.1029/2005JD006947.

Leovy, C. B., C.-R. Sun, M. H. Hitchman, E. E. Remsberg, J. M. Russell III, L. L. Gordley, J. C. Gille, and L. V. Lyjak, 1985: Transport of ozone in the middle stratosphere: Evidence for planetary wave breaking. *J. Atmos. Sci.*, **42**, 230–244, https://doi.org/10.1175/1520-0469(1985)042<0230:TOOITM>2.0.CO;2.

Liebmann, B., and D. L. Hartmann, 1984: An observational study of tropical–midlatitude interaction on intraseasonal time scales during winter. *J. Atmos. Sci.*, **41**, 3333–3350, https://doi.org/10.1175/1520-0469(1984)041<3333:AOSOTI>2.0.CO;2.

Mantua, N. J., and S. R. Hare, 1997: PDO index. JISAO, accessed 10 November 2017, https://jisao.uw.edu/pdo/PDO.latest.txt.

——, ——, Y. Zhang, J. M. Wallace, and R. C. Francis, 1997: A Pacific interdecadal climate oscillation with impacts on salmon production. *Bull. Amer. Meteor. Soc.*, **78**, 1069–1079, https://doi.org/10.1175/1520-0477(1997)078<1069:APICOW>2.0.CO;2.

Martius, O., E. Zenklusen, C. Schwierz, and H. C. Davies, 2006: Episodes of Alpine heavy precipitation with an overlying elongated stratospheric intrusion: A climatology. *Int. J. Climatol.*, **26**, 1149–1164, https://doi.org/10.1002/joc.1295.

——, C. Schwierz, and H. C. Davies, 2007: Breaking waves at the tropopause in the wintertime Northern Hemisphere: Climatological analyses of the orientation and the theoretical LC1/2 classification. *J. Atmos. Sci.*, **64**, 2576–2592, https://doi.org/10.1175/JAS3977.1.

Massacand, A. C., H. Wernli, and H. C. Davies, 1998: Heavy precipitation on the alpine southside: An upper-level precursor. *Geophys. Res. Lett.*, **25**, 1435–1438, https://doi.org/10.1029/98GL50869.

McIntyre, M. E., and T. N. Palmer, 1983: Breaking planetary waves in the stratosphere. *Nature*, **305**, 593–600, https://doi.org/10.1038/305593a0.

——, and ——, 1984: The 'surf zone' in the stratosphere. *J. Atmos. Terr. Phys.*, **46**, 825–849, https://doi.org/10.1016/0021-9169(84)90063-1.

Nigam, S., M. Barlow, and E. H. Berbery, 1999: Analysis links Pacific decadal variability to drought and streamflow in United States. *Eos, Trans. Amer. Geophys. Union*, **80**, 621–625, https://doi.org/10.1029/99EO00412.

O'Reilly, C. H., and A. Czaja, 2015: The response of the Pacific storm track and atmospheric circulation to Kuroshio Extension variability. *Quart. J. Roy. Meteor. Soc.*, **141**, 52–66, https://doi.org/10.1002/qj.2334.

Peters, D., and D. W. Waugh, 1996: Influence of barotropic shear on the poleward advection of upper-tropospheric air. *J. Atmos. Sci.*, **53**, 3013–3031, https://doi.org/10.1175/1520-0469(1996)053<3013:IOBSOT>2.0.CO;2.

Plumb, R. A., 1985: On the three-dimensional propagation of stationary waves. *J. Atmos. Sci.*, **42**, 217–229, https://doi.org/10.1175/1520-0469(1985)042<0217:OTTDPO>2.0.CO;2.

Postel, G. A., and M. H. Hitchman, 1999: A climatology of Rossby wave breaking along the subtropical tropopause. *J. Atmos. Sci.*, **56**, 359–373, https://doi.org/10.1175/1520-0469(1999)056<0359:ACORWB>2.0.CO;2.

——, and ——, 2001: A case study of Rossby wave breaking along the subtropical tropopause. *Mon. Wea. Rev.*, **129**, 2555–2569, https://doi.org/10.1175/1520-0493(2001)129<2555:ACSORW>2.0.CO;2.

Qiu, B., 2003: Kuroshio Extension variability and forcing of the Pacific decadal oscillations: Responses and potential feedback. *J. Phys. Oceanogr.*, **33**, 2465–2482, https://doi.org/10.1175/2459.1.

Schneider, N., and B. D. Cornuelle, 2005: The forcing of the Pacific decadal oscillation. *J. Climate*, **18**, 4355–4373, https://doi.org/10.1175/JCLI3527.1.

Scott, R. K., and J.-P. Cammas, 2002: Wave breaking and mixing at the subtropical tropopause. *J. Atmos. Sci.*, **59**, 2347–2361, https://doi.org/10.1175/1520-0469(2002)059<2347:WBAMAT>2.0.CO;2.

Strong, C., and G. Magnusdottir, 2008: Tropospheric Rossby wave breaking and the NAO/NAM. *J. Atmos. Sci.*, **65**, 2861–2876, https://doi.org/10.1175/2008JAS2632.1.

Thompson, D. W. J., and J. M. Wallace, 2000: Annular modes in the extratropical circulation. Part I: Month-to-month variability. *J. Climate*, **13**, 1000–1016, https://doi.org/10.1175/1520-0442(2000)013<1000:AMITEC>2.0.CO;2.

Thorncroft, C. D., B. J. Hoskins, and M. E. McIntyre, 1993: Two paradigms of baroclinic-wave life-cycle behaviour. *Quart. J. Roy. Meteor. Soc.*, **119**, 17–55, https://doi.org/10.1002/qj.49711950903.

Tyrlis, E., and B. J. Hoskins, 2008: The morphology of Northern Hemisphere blocking. *J. Atmos. Sci.*, **65**, 1653–1665, https://doi.org/10.1175/2007JAS2338.1.

Waugh, D. W., 2005: Impact of potential vorticity intrusions on subtropical upper tropospheric humidity. *J. Geophys. Res.*, **110**, D11305, https://doi.org/10.1029/2004JD005664.

——, and L. M. Polvani, 2000: Climatology of intrusions into the tropical upper troposphere. *Geophys. Res. Lett.*, **27**, 3857–3860, https://doi.org/10.1029/2000GL012250.

Wernli, H., and M. Sprenger, 2007: Identification and ERA-15 climatology of potential vorticity streamers and cutoffs near the extratropical tropopause. *J. Atmos. Sci.*, **64**, 1569–1586, https://doi.org/10.1175/JAS3912.1.

Zhang, G., Z. Wang, T. J. Dunkerton, M. S. Peng, and G. Magnusdottir, 2016: Extratropical impacts on Atlantic tropical cyclone activity. *J. Atmos. Sci.*, **73**, 1401–1418, https://doi.org/10.1175/JAS-D-15-0154.1.

——, ——, M. S. Peng, and G. Magnusdottir, 2017: Characteristics and impacts of extratropical Rossby wave breaking during the Atlantic hurricane season. *J. Climate*, **30**, 2363–2379, https://doi.org/10.1175/JCLI-D-16-0425.1.

Zhang, Y., J. M. Wallace, and D. S. Battisti, 1997: ENSO-like interdecadal variability: 1900–93. *J. Climate*, **10**, 1004–1020, https://doi.org/10.1175/1520-0442(1997)010<1004:ELIV>2.0.CO;2.